2-D Electromagnetic Scattering and Inverse Scattering From Anisotropic Objects Under TE Illumination Solved by the Hybrid SIM/SEM

Jiawen Li, Zili Li, Zhen Guan, and Feng Han, *Senior Member, IEEE*

***Abstract*— This article presents an efficient hybrid solver based on the spectral-integral method (SIM) and the spectral element method (SEM) which is used to solve both the electromagnetic (EM) scattering and inverse scattering by two-dimensional (2-D) anisotropic objects when the excitation source is transverse electric (TE_z)-polarized. The scalar Helmholtz equation describing the magnetic field variation inside the anisotropic region is discretized and solved by SEM and the corresponding computational domain is truncated by a smooth elliptical surface on which SIM is implemented to fulfill the radiation boundary condition (RBC). The scattered EM fields at the receiver array are directly computed by multiplying the spectral-domain solution of the EM fields on the elliptical boundary and the spectral-domain radiation matrix. In the inverse scattering, the sensitivity matrix is constructed by multiplying the adjoint solution of magnetic fields by the first-order derivatives of the system stiffness matrix with respect to anisotropic model parameters inside the inversion domain. Meanwhile, in each iteration, the sensitivity matrix is synchronously updated based on the solution of the forward solver in the last iteration step. Numerical experiments are carried out to show the computation efficiency and correctness of both the scattering and inverse scattering solvers based on the hybrid SIM/SEM.**

***Index Terms*— Conjugate gradient (CG), electromagnetic (EM) scattering and inverse scattering, spectral element method (SEM), spectral-integral method (SIM).**

I. Introduction

ELECTROMAGNETIC (EM) scattering and inverse scattering are two reciprocal processes that are ubiquitous in both military and civil areas. The forward scattering refers to computing the spatial EM field distribution when the incident wave interacts with specific targets, which has been intensively studied in the past decades for the applications of remote sensing [1], nondestructive testing [2], metamaterial design [3], and so on. By contrast, the inverse scattering is to infer the model parameters, for example, dielectric permittivity, conductivity, positions, and sizes, of the unknown targets from measured EM fields by some iterative methods. Typical applications include microwave imaging [4], geophysical exploration [5], biomedical diagnosis [6], and so on.

One of the commonly used methods to solve EM scattering and inverse scattering problems is using the integral equation (IE). The total EM fields inside the computational domain when the scatterers are present are regarded as the summation of the incident EM fields when the scatterers are absent and the scattered EM fields that are radiated by the fictitious equivalent current generated by the total fields inside the computational domain. Therefore, there is no analytical solution for such an equation. The earliest used approach is to discretize the IE and numerically solve it using the method of moment (MoM) [7], [8]. Nevertheless, MoM has an unaffordable computational cost if the scatterer has a large electrical size [9]. A series of fast algorithms such as stabilized biconjugate gradient (BCGS) fast Fourier transform (FFT) [10], multilevel fast multipole algorithm (MLFMA) [11], adaptive integral method (AIM) [12], and precorrected-FFT (pFFT) [13] are suggested to lower the computational cost of MoM. The fast computation is achieved by these methods through utilizing FFT to accelerate the convolution in the discretized IEs, for example, BCGS-FFT, or through dividing the computation domain into the near-field part and the far-field part, for example, MLFMA, AIM, and pFFT. The full-wave inversion (FWI) solvers which iteratively call these fast-forward scattering algorithms have also been intensively studied in the past decades and applied in various EM detection scenarios. For example, the Born-type iterative methods have been combined with the BCGS-FFT forward solver to reconstruct three-dimensional (3-D) biaxial anisotropic objects [14], 3-D arbitrary anisotropic objects [15], [16], or deep Earth ore distribution from airborne EM measurement [17]. On the other hand, there are also some FWI solvers based on the IEs but without calling the forward solvers. For example, in the contrast source inversion (CSI), the cost function is constructed using the summation of mismatches in the data equation and the state equation which is usually described by an IE [18]. When it is implemented, the induced

Manuscript received 4 September 2023; revised 26 January 2024; accepted 4 February 2024. Date of publication 13 February 2024; date of current version 9 April 2024. This work was supported by the National Natural Science Foundation of China under Grant 62271428. *(Corresponding author: Feng Han.)*

Jiawen Li and Zili Li are with the School of Electronic and Information Engineering, Guangxi Normal University, Guangxi 541004, China (e-mail: jiawenli@mailbox.gxnu.edu.cn; zlienishi@mailbox.gxnu.edu.cn).

Zhen Guan is with the School of Science, Tianjin University of Technology, Tianjin 300384, China (e-mail: zguan@email.tjut.edu.cn).

Feng Han is with the School of Computing and Information Technology, Great Bay University, Guangdong 523000, China, and also with the Institute of Electromagnetics and Acoustics, Xiamen University, Xiamen 361005, China (e-mail: feng.han@gbu.edu.cn; feng.han@xmu.edu.cn).

Color versions of one or more figures in this article are available at https://doi.org/10.1109/TAP.2024.3363458.

Digital Object Identifier 10.1109/TAP.2024.3363458

current and the dielectric contrast are alternately updated [19]. The subspace-based optimization method (SOM) is carried similar to CSI but for a subspace of the induced current [20]. The advantages of these IE-based EM scattering and inverse scattering methods lie in the restricted computation domain. The scatterers can be tightly wrapped by the computation domain boundary and the EM wave propagation between the computation domain and the transceivers is usually described by Green's functions. However, the drawback is also obvious. The Green's functions for the background medium must be precisely evaluated, no matter analytically or numerically. This is usually difficult for an arbitrary inhomogeneous background.

EM scattering and inverse scattering methods based on differential equation (DE), for example, Helmholtz equation, can naturally overcome this drawback since the whole computational domain, no matter whether a homogeneous one or an arbitrary inhomogeneous one, which wraps the transceivers, can be completely discretized, and thus the EM fields at any point inside the domain can be directly solved when the DE is constrained by some boundary conditions. One of the most common applications of DE-based forward solvers is simulating EM scattering from anomalous bodies, for example, metal minerals and underground water, which are buried in inhomogeneous deep Earth with irregular topography. For example, in [21], the finite-element method (FEM) with distorted hexahedral grids is adopted to simulate magnetotelluric signals in the Xinjiang Luntai area when the surface topography is incorporated in the forward model. In [22], the finite-difference (FD) method is taken to compute 2.5-D EM scattering for logging-while-drilling measurements in complex geological scenarios. In [23], the 3-D spectral element method (SEM) with unstructured hexahedral meshes is used to simulate controlled-source EM data. The FWI methods corresponding to these common DE-based forward scattering methods include the quasi-Newton (QN) method [24], conjugate-gradient (CG) method [25], nonlinear CG (NLCG) method [26], Gauss–Newton (GN) method [21], and so on. And these methods have been successfully applied to 2-D [27], 2.5-D [28], and 3-D [29] geophysical inversion in which the computational domain is usually truncated by absorption boundaries.

In our previous work, we have accomplished the EM forward scattering computation [30] based on SEM and the inverse scattering computation [31] based on SEM-CG but with the computational domain truncated by the radiation boundary condition (RBC) which are formulated by the spectral integral method (SIM). This hybrid spectral-element spectral-integral (SESI) method inherits the merits of both SEM and SIM, and thus the EM fields inside the computation domain are solved by the DE-based SEM but the transceivers are allowed to be placed far away from the computation domain. However, in [30] and [31], only dielectric isotropic scatterers are considered. Meanwhile, the SIM can only be implemented on a circular smooth boundary. Therefore, we extend our previous works and make three new contributions here: 1) the EM waves are excited and scattered in the transverse electric (TE_z) mode, which leads to a different spectral-domain system matrix and a different radiation matrix compared with those in [30] and [31]; 2) the 2-D scatterers are allowed to be biaxially anisotropic or arbitrary anisotropic, which leads to a completely different sensitivity matrix used in the inversion; and 3) SIM is allowed to be implemented on a smooth elliptical boundary. In addition, one should note our work is different from [32], [33], and [34] since the forward and inverse solvers used in these works are based on IEs. However, both solvers in our work are based on DEs which are solved by the hybrid SIM/SEM. Our work is also different from [35] since only the SIM is used to solve the EM scattering from multilayered anisotropic ellipses in [35].

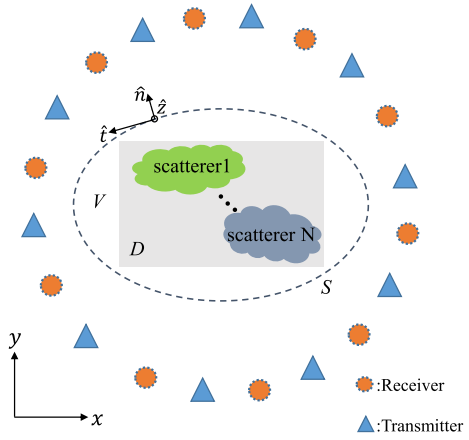

Fig. 1. Two-dimensional EM scattering and inverse scattering model based on the hybrid SIM/SEM. The forward scattering is implemented inside the domain V which is wrapped by a smooth elliptical boundary S. The inverse scattering is implemented in the region D embedded inside V. The transmitter can either be a 2-D magnetic dipole or a plane wave with TE_z polarization.

The rest of this article is organized as follows. In Section II, the detailed mathematical formulas of the 2-D SEM and the hybrid SESI method for the TE_z mode are first presented. Then, the first-order sensitivity matrix of the scattered EM fields recorded at the receiver array with respect to multiple dielectric anisotropic parameters inside the computational domain is derived in detail. Finally, the implementation of the FWI based on the SESI forward solver is simply mentioned. In Section III, the accuracy and efficiency of the forward SESI solver is verified by comparing its computation results with those from the traditional FEM carried out by the commercial software COMSOL. In Section IV, two numerical examples are given to show the feasibility of the SESI-CG to simultaneously reconstruct multiple anisotropic parameters. Finally, in Section V, the conclusion is drawn.

II. Problem Formulation

As shown in Fig. 1, several anisotropic scatterers are placed inside the inversion domain D which is wrapped by the elliptical boundary S. The SIM is implemented on S and the forward scattering is solved by SEM in the region V. By contrast, the FWI is only performed in the domain D. The TE_z-polarized transmitter can be a plane wave with the E_x, E_y, and H_z components or a 2-D magnetic dipole. The major contents presented in this section are different from those presented in [31, Sec. II] since we consider the anisotropy and the 2-D TE_z EM wave mode in this work. We first give the brief formulas of SEM for the TE_z EM wave mode. Then,

the combination of SEM with SIM in the forward scattering computation is discussed in detail. Following is the detailed derivation of the first-order sensitivity matrix for the TE_z EM mode. Finally, the FWI based on the CG method is briefly mentioned.

A. 2-D SEM for the TE_z Mode

For the 2-D TE_z EM wave mode, the scalar Helmholtz equation based on the magnetic fields can be written as

$$-\nabla_t \times \left(\bar{\bar{\epsilon}}_t^{-1} \nabla_t \times \hat{z} H_z\right) + k_0^2 \mu \hat{z} H_z = \hat{z} S_h \tag{1}$$

where $\nabla_t = \hat{x}(\partial/\partial x) + \hat{y}(\partial/\partial y)$ is the gradient operator in the xy plane, $k_0 = \omega\sqrt{\varepsilon_0 \mu_0}$ is the wavenumber of vacuum, and S_h is the magnetic current source inside the computational domain V. Since we consider the dielectric anisotropy of the scatterers, the complex relative permittivity tensor $\bar{\bar{\epsilon}}_t$ is defined as

$$\begin{aligned}\bar{\bar{\epsilon}}_t &= \begin{bmatrix} \epsilon_{xx} & \epsilon_{xy} \\ \epsilon_{yx} & \epsilon_{yy} \end{bmatrix} = \mathbf{\Theta}^{-1} \begin{bmatrix} \epsilon_x & 0 \\ 0 & \epsilon_y \end{bmatrix} \mathbf{\Theta} \\ &= \mathbf{\Theta}^{-1} \begin{bmatrix} \varepsilon_x + \dfrac{\sigma_x}{j\omega\varepsilon_0} & 0 \\ 0 & \varepsilon_y + \dfrac{\sigma_y}{j\omega\varepsilon_0} \end{bmatrix} \mathbf{\Theta}\end{aligned} \tag{2}$$

where

$$\mathbf{\Theta} = \begin{bmatrix} \cos\theta & \sin\theta \\ -\sin\theta & \cos\theta \end{bmatrix} \tag{3}$$

is the rotation matrix in which θ is the angle between the optical axis of the biaxially anisotropic medium and the positive $\hat{x}$-axis [32]. We then use the scalar Gauss–Lobatto–Legendre (GLL) testing function $\hat{z}\psi_p$ [36] to test both sides of (1) and conduct a series of mathematical transforms based on some vector identities and physical laws and finally come to the weak form

$$\begin{aligned}\int_V \left[-(\hat{z} \times \nabla_t \psi_p) \cdot \bar{\bar{\epsilon}}_t^{-1} (\hat{z} \times \nabla_t H_z) + k_0^2 \mu \psi_p H_z\right] dx dy \\ + jk_0 \int_S \psi_p \overline{M}_z(t) dt = \int_V \psi_p S_h dx dy\end{aligned} \tag{4}$$

where $\overline{M}_z = (1/\eta_0) M_z$ is the normalized surface magnetic current density on the boundary S. On the other hand, we will use the Galerkin method in this work and thus expand H_z in the inhomogeneous region V and on the boundary S and $\overline{M}$ on the boundary S also by GLL basis functions

$$H_z \approx \sum_{q=1}^{N_i} h_q^i \psi_q(x, y) + \sum_{q=1}^{N_b} h_q^b \psi_q(x, y) \tag{5a}$$

$$\overline{M}_z \approx \sum_{q=1}^{N_b} \overline{m}_q^b \psi_q(t) \tag{5b}$$

where the superscript i means inside the region V, the superscript b means on the boundary S, N_i denotes the discretized quadrilateral element number inside V, and N_b is the discretized node number on S. One should note that there is no source inside the computation domain V. Therefore, substituting (5) into (4), performing the integration, and discarding the source term yield the discretized algebraic equation

$$\begin{bmatrix} \mathbf{Z}^{ii} & \mathbf{Z}^{ib} & \mathbf{0} \\ \mathbf{Z}^{bi} & \mathbf{Z}^{bb} & \mathbf{Z}_S \end{bmatrix} \begin{bmatrix} \mathbf{h}^i \\ \mathbf{h}^b \\ \overline{\mathbf{M}}^b \end{bmatrix} = \begin{bmatrix} \mathbf{0} \\ \mathbf{0} \end{bmatrix} \tag{6}$$

where $\mathbf{h}^i = (h_q^i)_{q=1}^{N_i}$, $\mathbf{h}^b = (h_q^b)_{q=1}^{N_b}$, and $\overline{\mathbf{M}}^b = (\overline{m}_q^b)_{q=1}^{N_b}$ are the expansion coefficient matrices for magnetic fields inside V, magnetic fields on the boundary S, and normalized magnetic current density on S, respectively. The elements of matrices $\mathbf{Z}^{ii}$, $\mathbf{Z}^{ib} = (\mathbf{Z}^{bi})^T$, $\mathbf{Z}^{bb}$, and $\mathbf{Z}_S$ are evaluated by

$$Z_{pq}^{uv} = \int_V \left[-(\hat{z} \times \nabla_t \psi_p) \cdot \bar{\bar{\epsilon}}_t^{-1} (\hat{z} \times \nabla_t \psi_q) + k_0^2 \mu \psi_p \psi_q\right] dx dy \tag{7a}$$

$$Z_{S,pq} = jk_0 \int_S \psi_p \psi_q(t) dt \tag{7b}$$

where the subscripts p and q, respectively, indicate the row index and column index of the element Z in the matrix $\mathbf{Z}^{uv}$ or $\mathbf{Z}_S$. The superscripts u and v can take the value either of i or b, which means the pth testing function and the qth basis function are located inside the domain V or on the boundary S. Equation (6) is actually the discretized algebraic form of the 2-D Helmholtz equation in the TE_z mode. Unfortunately, it cannot be directly solved because the boundary condition is not clarified. In the following, SIM applied to the smooth elliptical boundary S fulfilling the RBC is used to truncate the computational domain V.

B. Hybrid SESI Methods for the TE_z Mode

According to the surface equivalence theorem, the surface IE for magnetic fields on the boundary S can be written as

$$\begin{aligned}\frac{1}{2}\hat{z} H_z(\boldsymbol{\rho}) - \oint_S \bar{\bar{\mathbf{G}}}_{\mathbf{HJ}}(\boldsymbol{\rho}, \boldsymbol{\rho}') \cdot \left[\hat{n}(\boldsymbol{\rho}') \times \hat{z} H_z(\boldsymbol{\rho}')\right] dt' \\ - \oint_S \bar{\bar{\mathbf{G}}}_{\mathbf{HM}}(\boldsymbol{\rho}, \boldsymbol{\rho}') \cdot \hat{z} M_z(\boldsymbol{\rho}') dt' = \hat{z} H_z^{inc}(\boldsymbol{\rho})\end{aligned} \tag{8}$$

where $\oint$ is the Cauchy principal integral used to circumvent the singularity when the source point $\boldsymbol{\rho}'$ and the field point $\boldsymbol{\rho}$ overlap on S, $\hat{n}$ is the outward unit normal vector along the elliptical boundary as shown in Fig. 1, and $\bar{\bar{\mathbf{G}}}_{\mathbf{HJ}}$ and $\bar{\bar{\mathbf{G}}}_{\mathbf{HM}}$ are 2-D Green's functions whose expressions are given in [35, Appendix A]. Since the boundary S is smooth, we can adopt the SIM presented in [35] and [37] and implement the integration of (8) in the spectral domain. As a result, (8) can be discretized and compactly written as

$$\mathbf{Z}_J \widetilde{\mathbf{h}}^b + \mathbf{Z}_M \widetilde{\overline{\mathbf{M}}}^b = \mathbf{V}_S \tag{9}$$

where the superscript b denotes the boundary S, $\widetilde{\mathbf{h}}^b$ is the Fourier coefficient matrix of H_z on S, and its dimensions are $N_s \times N_T$, where N_s is the order of the Fourier series and N_T is the transmitter number, $\widetilde{\overline{\mathbf{M}}}^b$ is the Fourier coefficient matrix of normalized M_z on S with the dimensions of $N_s \times N_T$, $\mathbf{Z}_J$, and $\mathbf{Z}_M$ are, respectively, the Fourier expressions of $\bar{\bar{\mathbf{G}}}_{\mathbf{HJ}}$ and $\bar{\bar{\mathbf{G}}}_{\mathbf{HM}}$ with the dimensions of $N_s \times N_s$, and $\mathbf{V}_S$ is the matrix

composed of spatial-domain incident magnetic fields on the boundary S and has the dimensions of $N_s \times N_T$. Three points must be emphasized here: 1) since SIM has an exponential accuracy with a low spatial sampling density (SD) [35], there are usually more discretized points of SEM than those of SIM on the boundary S. In other words, N_b is much larger than N_s in our problem; 2) the discretized points of SIM must be completely included in those of SEM on S. Such a mandatory constraint is to guarantee the accurate forward and inverse Fourier transforms between the spatial-domain field values from SEM and the spectral-domain coefficients from SIM on the boundary S; and 3) to couple SIM and SEM on the boundary S, we use [35]

$$h^b(\theta_q) = \sum_{n=-\frac{N_s}{2}}^{\frac{N_s}{2}-1} \widetilde{h}_n^b e^{-jn\theta_q} \tag{10a}$$

$$\overline{m}^b(\theta_q) = \sum_{n=-\frac{N_s}{2}}^{\frac{N_s}{2}-1} \widetilde{\overline{m}}_n^b e^{-jn\theta_q} \tag{10b}$$

where θ_q is the azimuthal angle of the qth discretized point of SEM on S and n is the order of the Fourier series of H_z and normalized M_z on S from SIM. Equation (10) can be compactly written as

$$\mathbf{h}^b = \mathbf{T}\widetilde{\mathbf{h}}^b \tag{11a}$$

$$\overline{\mathbf{M}}^b = \mathbf{T}\widetilde{\overline{\mathbf{M}}}^b \tag{11b}$$

where $\mathbf{T}$ is the inverse Fourier transform matrix and has the dimensions of $N_b \times N_s$. Note $\mathbf{T}$ is not a square matrix since $N_b \gg N_s$ in our problem. We then substitute (11) into (6), combine (6) and (9), and obtain the matrix-form discretized state equation

$$\mathbf{Zh} = \mathbf{V} \tag{12}$$

where

$$\mathbf{Z} = \begin{bmatrix} \mathbf{Z}^{ii} & \mathbf{Z}^{ib}\mathbf{T} & \mathbf{0} \\ \mathbf{Z}^{bi} & \mathbf{Z}^{bb}\mathbf{T} & \mathbf{Z}_S\mathbf{T} \\ \mathbf{0} & \mathbf{Z}_J & \mathbf{Z}_M \end{bmatrix} \tag{13a}$$

$$\mathbf{h} = \begin{bmatrix} \mathbf{h}^i \\ \widetilde{\mathbf{h}}^b \\ \widetilde{\overline{\mathbf{M}}}^b \end{bmatrix} \tag{13b}$$

$$\mathbf{V} = \begin{bmatrix} \mathbf{0} \\ \mathbf{0} \\ \mathbf{V}_S \end{bmatrix} \tag{13c}$$

and the system matrix $\mathbf{Z}$ has the dimensions of $(N_i + N_b + N_s) \times (N_i + 2 \times N_s)$. Each column of $\mathbf{h}$ corresponds to the solution for each transmitter illumination. Since $N_b \gg N_s$ in our problem, the state equation (12) is overdetermined. In addition, the rank of the matrix $\mathbf{Z}$ is equal to its column number and thus the solution of $\mathbf{h}$ is unique. By multiplying the conjugate transpose of the system matrix in both sizes of (12), we obtain

$$\mathbf{Z}^H\mathbf{Zh} = \mathbf{Z}^H\mathbf{V}. \tag{14}$$

Therefore, the solution of the state equation (12) is

$$\mathbf{h} = (\mathbf{Z}^H\mathbf{Z})^{-1}\mathbf{Z}^H\mathbf{V}. \tag{15}$$

Once the EM field values on the boundary S are obtained, the scattered fields at the receiver array are evaluated by the data equations

$$\mathbf{E}^{sct}(\boldsymbol{\rho}_r) = \oint_S \overline{\overline{\mathbf{G}}}_{\mathbf{EJ}}(\boldsymbol{\rho}_r, \boldsymbol{\rho}') \cdot \left[\hat{n}(\boldsymbol{\rho}') \times \hat{z}H_z(\boldsymbol{\rho}')\right]dt' + \oint_S \overline{\overline{\mathbf{G}}}_{\mathbf{EM}}(\boldsymbol{\rho}_r, \boldsymbol{\rho}') \cdot \hat{z}M_z(\boldsymbol{\rho}')dt' \tag{16a}$$

$$\hat{z}H_z^{sct}(\boldsymbol{\rho}_r) = \oint_S \overline{\overline{\mathbf{G}}}_{\mathbf{HJ}}(\boldsymbol{\rho}_r, \boldsymbol{\rho}') \cdot \left[\hat{n}(\boldsymbol{\rho}') \times \hat{z}H_z(\boldsymbol{\rho}')\right]dt' + \oint_S \overline{\overline{\mathbf{G}}}_{\mathbf{HM}}(\boldsymbol{\rho}_r, \boldsymbol{\rho}') \cdot \hat{z}M_z(\boldsymbol{\rho}')dt' \tag{16b}$$

where the specific expressions of Green's functions are given in [35, Appendix A]. We suppose there are N_T transmitters and N_R receivers. Equation (16) can be further written in matrix forms

$$\mathbf{E}_x^{sct} = \begin{bmatrix} \mathbf{0} & \mathbf{R}_J^{E_x} & \mathbf{R}_M^{E_x} \end{bmatrix} \begin{bmatrix} \mathbf{h}^i \\ \mathbf{h}^b \\ \overline{\mathbf{M}}^b \end{bmatrix} \tag{17a}$$

$$\mathbf{E}_y^{sct} = \begin{bmatrix} \mathbf{0} & \mathbf{R}_J^{E_y} & \mathbf{R}_M^{E_y} \end{bmatrix} \begin{bmatrix} \mathbf{h}^i \\ \mathbf{h}^b \\ \overline{\mathbf{M}}^b \end{bmatrix} \tag{17b}$$

$$\mathbf{H}_z^{sct} = \begin{bmatrix} \mathbf{0} & \mathbf{R}_J^{H_z} & \mathbf{R}_M^{H_z} \end{bmatrix} \begin{bmatrix} \mathbf{h}^i \\ \mathbf{h}^b \\ \overline{\mathbf{M}}^b \end{bmatrix} \tag{17c}$$

where the radiation matrix $\mathbf{R}$ composed of Green's functions has the dimensions of $N_R \times N_s$ and the scattered fields $\mathbf{E}_x^{sct}$, $\mathbf{E}_y^{sct}$, and $\mathbf{H}_z^{sct}$ have the same dimensions of $N_R \times N_T$. We then suppose each independent receiver is located in a fictitious smooth circle, expand both the radiation matrix $\mathbf{R}$ and the field values on the boundary S in (17) using Fourier series, take the similar measures as those in the state equation to derive (9) from (8), and finally come to the spectral-domain discretized data equations

$$\mathbf{E}_x^{sct} = \begin{bmatrix} \mathbf{0} & \widetilde{\mathbf{R}}_J^{E_x} & \widetilde{\mathbf{R}}_M^{E_x} \end{bmatrix} \begin{bmatrix} \mathbf{h}^i \\ \widetilde{\mathbf{h}}^b \\ \widetilde{\overline{\mathbf{M}}}^b \end{bmatrix} \tag{18a}$$

$$\mathbf{E}_y^{sct} = \begin{bmatrix} \mathbf{0} & \widetilde{\mathbf{R}}_J^{E_y} & \widetilde{\mathbf{R}}_M^{E_y} \end{bmatrix} \begin{bmatrix} \mathbf{h}^i \\ \widetilde{\mathbf{h}}^b \\ \widetilde{\overline{\mathbf{M}}}^b \end{bmatrix} \tag{18b}$$

$$\mathbf{H}_z^{sct} = \begin{bmatrix} \mathbf{0} & \widetilde{\mathbf{R}}_J^{H_z} & \widetilde{\mathbf{R}}_M^{H_z} \end{bmatrix} \begin{bmatrix} \mathbf{h}^i \\ \widetilde{\mathbf{h}}^b \\ \widetilde{\overline{\mathbf{M}}}^b \end{bmatrix}. \tag{18c}$$

Consequently, the scattered fields at the receiver array can be immediately obtained by substituting (15) into (18).

C. Assembly of the Sensitivity Matrix

Now let us discuss how to assemble the sensitivity matrix for FWI. We use the single-frequency scattered electric field

data to reconstruct the anisotropic permittivity $\bar{\bar{\epsilon}}_t$, that is, ε_x, ε_y, σ_x, σ_y, and θ in the inversion domain D. First, we assume the inversion domain D keeps at least one element away from the elliptical boundary S. Such an assumption is to lower the computation complexity for the evaluation of the sensitivity matrix since only $\mathbf{Z}^{ii}$ in (13a) depends on the unknown model parameters inside D if it is not in contact with S. In addition, the inverse Fourier transform matrix $\mathbf{T}$ in (13a) and the radiation matrix $\mathbf{R}$ in (18) are also independent of the unknown model parameters to be reconstructed. We assume those model parameters are assembled into a vector $\mathbf{X}$ and rewrite the data equations (18a) and (18b) compactly as

$$\mathbf{F}^{sct} = \mathbf{R}\mathbf{h} \tag{19}$$

where $\mathbf{F}^{sct}$ can be $\mathbf{E}_x^{sct}$ or $\mathbf{E}_y^{sct}$. Taking the derivatives of both sides of (19) with respect to $\mathbf{X}$

$$\frac{\partial \mathbf{F}^{sct}}{\partial \mathbf{X}} = \mathbf{R}\frac{\partial \mathbf{h}}{\partial \mathbf{X}} \tag{20}$$

and also taking the derivatives of both sides of (12) with respect to $\mathbf{X}$

$$\frac{\partial \mathbf{Z}}{\partial \mathbf{X}}\mathbf{h} + \mathbf{Z}\frac{\partial \mathbf{h}}{\partial \mathbf{X}} = \mathbf{0} \tag{21}$$

and multiplying the conjugate transpose of the system matrix $\mathbf{Z}$ by (21)

$$\mathbf{Z}^H\frac{\partial \mathbf{Z}}{\partial \mathbf{X}}\mathbf{h} + \mathbf{Z}^H\mathbf{Z}\frac{\partial \mathbf{h}}{\partial \mathbf{X}} = \mathbf{0} \tag{22}$$

we finally obtain

$$\frac{\partial \mathbf{h}}{\partial \mathbf{X}} = -\left(\mathbf{Z}^H\mathbf{Z}\right)^{-1}\mathbf{Z}^H\frac{\partial \mathbf{Z}}{\partial \mathbf{X}}\mathbf{h} \tag{23}$$

in which $\mathbf{Z}^H\mathbf{Z}$ is an invertible square matrix. Finally, we substitute (23) into (20) and take the transposes of both sides and come to

$$\left(\frac{\partial \mathbf{F}^{sct}}{\partial \mathbf{X}}\right)^T = -\left(\frac{\partial \mathbf{Z}}{\partial \mathbf{X}}\mathbf{h}\right)^T\left(\mathbf{Z}^H\right)^T\left[\left(\mathbf{Z}^H\mathbf{Z}\right)^T\right]^{-1}\mathbf{R}^T \tag{24}$$

where we have interchanged the order of matrix inverse and transpose. Now, let $[(\mathbf{Z}^H\mathbf{Z})^T]^{-1}\mathbf{R}^T = \mathbf{h}^*$ denote the adjoint magnetic field solution for which $(\mathbf{Z}^H\mathbf{Z})^T$ is the new system matrix. Meanwhile, keep in mind the adjoint solution depends on the fictitious excitation source $\mathbf{E}_x^{sct}$ or $\mathbf{E}_y^{sct}$. By substituting $\mathbf{h}^*$ into (24) and taking the transposes of both sides again, we obtain

$$\frac{\partial \mathbf{F}^{sct}}{\partial \mathbf{X}} = -(\mathbf{h}^*)^T\mathbf{Z}^H\frac{\partial \mathbf{Z}}{\partial \mathbf{X}}\mathbf{h}. \tag{25}$$

Then, let us discuss how to compute $(\partial\mathbf{Z}/\partial\mathbf{X})$ in (25). Assume the complex relative permittivity ϵ_x, ϵ_y, or the rotation angle θ in the mth quadrilateral element is denoted by x_m. Since $(\partial\mathbf{Z}/\partial x_m)$ is only related to the stiffness matrix, we now transform the first term of the integration in (7a) from the physical coordinate to the reference coordinate

$$\begin{aligned} Z_{pq}^{ii} &= \int_V -(\hat{z}\times\nabla_t\psi_p(x,y))\cdot\bar{\bar{\epsilon}}_t^{-1}(\hat{z}\times\nabla_t\psi_q(x,y))dxdy \\ &= \int_\Lambda -\left(\hat{z}\times\mathbf{J}^{-1}\nabla_t'\phi(\xi,\eta)\right)\cdot\bar{\bar{\epsilon}}_t^{-1}\left(\hat{z}\times\mathbf{J}^{-1}\nabla_t'\phi(\xi,\eta)\right)|\mathbf{J}|d\xi d\eta \end{aligned} \tag{26}$$

where ξ is the abscissa of the reference coordinate, η is the ordinate of the reference coordinate, $\mathbf{J} = \mathbf{J}(\xi,\eta)$ is the Jacobian matrix for coordinate system transform, $|\mathbf{J}|$ is its determinant, $\phi(\xi,\eta)$ represents the basis function or testing function in the reference coordinate system, and $\nabla_t' = \hat{\xi}(\partial/\partial\xi) + \hat{\eta}(\partial/\partial\eta)$ is the gradient operator in the $\xi\eta$ domain. Since we only consider the second SEM in this work, the basis function or the testing function in (26) can be replaced with one of the nine GLL functions. As a result, (26) can be rewritten as

$$\begin{aligned} Z_{pq}^{ii}(i,j) = \int_{-1}^{1}\int_{-1}^{1} &-\left(\hat{z}\times\mathbf{J}^{-1}\nabla_t'\phi_i(\xi,\eta)\right) \\ &\cdot\bar{\bar{\epsilon}}_t^{-1}\left(\hat{z}\times\mathbf{J}^{-1}\nabla_t'\phi_j(\xi,\eta)\right)|\mathbf{J}(\xi,\eta)|d\xi d\eta \end{aligned} \tag{27}$$

where $i \in [1,9]$ is the index of the GLL testing function in the reference domain for ψ_p while $j \in [1,9]$ is the index of the GLL basis function in the reference domain for ψ_q. In addition, $\hat{z}\times$ actually can be replaced with $\left[\begin{smallmatrix}0 & -1\\ 1 & 0\end{smallmatrix}\right]\cdot$ for a 2-D problem and the double integrals in (27) can be numerically evaluated using the GLL quadrature. Therefore, we have

$$\begin{aligned} &Z_{pq}^{ii}(i,j) \\ &= \sum_{k=1}^{9} -\left(\begin{bmatrix}0 & -1\\ 1 & 0\end{bmatrix}\cdot\left[\mathbf{J}^{-1}\nabla_t'\phi_i\right]_{\xi_k,\eta_k}\right) \\ &\quad\cdot\bar{\bar{\epsilon}}_t^{-1}\left(\begin{bmatrix}0 & -1\\ 1 & 0\end{bmatrix}\cdot\left[\mathbf{J}^{-1}\nabla_t'\phi_j\right]_{\xi_k,\eta_k}\right)|\mathbf{J}(\xi_k,\eta_k)|w_{k_\xi}w_{k_\eta} \end{aligned} \tag{28}$$

where k is the index for 2-D GLL quadrature point and w_{k_ξ} and w_{k_η} are the corresponding weights in two orthogonal directions, respectively. Obviously, $(\partial Z_{pq}^{ii}/\partial x_m)$ completely depends on $(\partial\bar{\bar{\epsilon}}_t^{-1}/\partial x_m)$. And it is not difficult to prove

$$\frac{\partial\bar{\bar{\epsilon}}_t^{-1}}{\partial\epsilon_x} = \mathbf{\Theta}^{-1}\begin{bmatrix}-\frac{1}{\epsilon_x^2} & 0\\ 0 & 0\end{bmatrix}\mathbf{\Theta} = \mathbf{\Theta}^{-1}\boldsymbol{\epsilon}_x^{eq}\mathbf{\Theta} \tag{29a}$$

$$\frac{\partial\bar{\bar{\epsilon}}_t^{-1}}{\partial\epsilon_y} = \mathbf{\Theta}^{-1}\begin{bmatrix}0 & 0\\ 0 & -\frac{1}{\epsilon_y^2}\end{bmatrix}\mathbf{\Theta} = \mathbf{\Theta}^{-1}\boldsymbol{\epsilon}_y^{eq}\mathbf{\Theta} \tag{29b}$$

$$\frac{\partial\bar{\bar{\epsilon}}_t^{-1}}{\partial\theta} = \mathbf{\Theta}^{-1}\begin{bmatrix}0 & \frac{1}{\epsilon_x}-\frac{1}{\epsilon_y}\\ \frac{1}{\epsilon_x}-\frac{1}{\epsilon_y} & 0\end{bmatrix}\mathbf{\Theta} = \mathbf{\Theta}^{-1}\boldsymbol{\theta}^{eq}\mathbf{\Theta} \tag{29c}$$

where the superscript "eq" means "equivalent." Specifically speaking, we can directly replace the original $\left[\begin{smallmatrix}\epsilon_x & 0\\ 0 & \epsilon_y\end{smallmatrix}\right]$ with the equivalent matrix $\boldsymbol{\epsilon}_x^{eq}$, $\boldsymbol{\epsilon}_y^{eq}$, or $\boldsymbol{\theta}^{eq}$ in $\mathbf{Z}^{ii}$ when we compute $(\partial Z_{pq}^{ii}/\partial x_m)$. Note $(\partial Z_{pq}^{ii}/\partial x_m)$ actually corresponds to one of the 9×9 elements most of whom are not equal to zero since the gradient ∇_t' acts on the basis and testing functions. Meanwhile, only the mth quadrilateral element of SEM affects the mth model parameter x_m. Therefore, the (i,j)th element of the derivatives of the mth quadrilateral element in Z_{pq}^{ii} with

respect to x_m can be evaluated by

$$\frac{\partial Z^{ii}_{pq,m}(i,j)}{\partial x_m} = \sum_{k=1}^{9} -\left(\begin{bmatrix}0 & -1\\ 1 & 0\end{bmatrix}\cdot\left[\mathbf{J}^{-1}\nabla_t'\phi_i\right]_{\xi_k,\eta_k}\right) \cdot \boldsymbol{\Theta}^{-1}\mathbf{m}^{eq}\boldsymbol{\Theta}\left(\begin{bmatrix}0 & -1\\ 1 & 0\end{bmatrix}\cdot\left[\mathbf{J}^{-1}\nabla_t'\phi_j\right]_{\xi_k,\eta_k}\right) \times |\mathbf{J}(\xi_k,\eta_k)|w_{k_\xi}w_{k_\eta} \tag{30}$$

where $\mathbf{m}^{eq}$ can be $\boldsymbol{\epsilon}_x^{eq}$, $\boldsymbol{\epsilon}_y^{eq}$, or $\boldsymbol{\theta}^{eq}$.

Finally, let us discuss how to compute $(\partial\mathbf{F}^{sct}/\partial\mathbf{X})$ in (25). For convenience, we take the scattered electric field $F^{sct}_{r,t}$ recorded by the rth receiver when the inversion domain D is illuminated by the tth transmitter as an example and only compute its derivative with respect to the mth quadrilateral element model parameter x_m here. In addition, we assume the nine GLL nodes of SEM in the mth quadrilateral element are numbered as $(p_1,\ldots,p_9)$ in all the nodes for the whole computation domain. Consequently, $(\partial Z^{ii}_{pq,m}(i,j)/\partial x_m)$ is placed in the position of (p_i,p_j) inside the whole matrix $(\partial\mathbf{Z}/\partial x_m)$. For the solution $\mathbf{h}_t$ of the state equation (15) when the inversion domain is illuminated by the tth transmitter, it only interacts with the elements placed in (p_i,p_j) of $(\partial\mathbf{Z}/\partial x_m)$ when we compute $(\partial\mathbf{Z}/\partial x_m)\mathbf{h}_t$. Therefore, the p_ith element in the vector $(\partial\mathbf{Z}/\partial x_m)\mathbf{h}_t$ is

$$\left(\frac{\partial\mathbf{Z}}{\partial x_m}\mathbf{h}_t\right)_{p_i} = \sum_{j=1}^{9}\frac{\partial Z^{ii}_{pq,m}(i,j)}{\partial x_m}(\mathbf{h}_t)_{p_j} \tag{31}$$

where $(\partial\mathbf{Z}/\partial x_m)\mathbf{h}_t$ has the dimensions of $(N_i+N_b+N_s)\times 1$ and only the nine elements located at $(p_1,\ldots,p_9)$ are not zero. Consequently, when we multiply $\mathbf{Z}^H$ by $(\partial\mathbf{Z}/\partial x_m)\mathbf{h}_t$, it only interacts with these nine nonzero elements. The lth element of $\mathbf{Z}^H((\partial\mathbf{Z}/\partial x_m)\mathbf{h}_t)$ is

$$\left[\mathbf{Z}^H\left(\frac{\partial\mathbf{Z}}{\partial x_m}\mathbf{h}_t\right)\right]_l = \sum_{i=1}^{9}(\mathbf{Z}^H)_{l,p_i}\sum_{j=1}^{9}\frac{\partial Z^{ii}_{pq,m}(i,j)}{\partial x_m}(\mathbf{h}_t)_{p_j} \tag{32}$$

where $\mathbf{Z}^H((\partial\mathbf{Z}/\partial x_m)\mathbf{h}_t)$ has the dimensions of $(N_i+2\times N_s)\times 1$. Finally, by substituting (30) into (32) and substituting (32) into (25), we obtain

$$\frac{\partial F^{sct}_{r,t}}{\partial x_m} = \sum_{l=1}^{N_i+2\times N_s}\left[(\mathbf{h}^*)^T\right]_{r,l}\sum_{i=1}^{9}(\mathbf{Z}^H)_{l,p_i} \times\sum_{j=1}^{9}\left\{\sum_{k=1}^{9}\left(\begin{bmatrix}0 & -1\\ 1 & 0\end{bmatrix}\cdot\left[\mathbf{J}^{-1}\nabla_t'\phi_i\right]_{\xi_k,\eta_k}\right)\cdot\boldsymbol{\Theta}^{-1}\mathbf{m}^{eq}\boldsymbol{\Theta} \cdot\left(\begin{bmatrix}0 & -1\\ 1 & 0\end{bmatrix}\cdot\left[\mathbf{J}^{-1}\nabla_t'\phi_j\right]_{\xi_k,\eta_k}\right)|\mathbf{J}(\xi_k,\eta_k)|w_{k_\xi}w_{k_\eta}\right\} \times(\mathbf{h}_t)_{p_j} \tag{33}$$

where whether F^{sct} takes E_x^{sct} or E_y^{sct} decides which electric field component is used to compute the adjoint field $\mathbf{h}^*$. Finally, we let m traverse all the quadrilateral elements of SEM, r traverse all receivers, and t traverse all transmitters and compute all $(\partial F^{sct}_{r,t}/\partial x_m)$ values to assemble the sensitivity matrix.

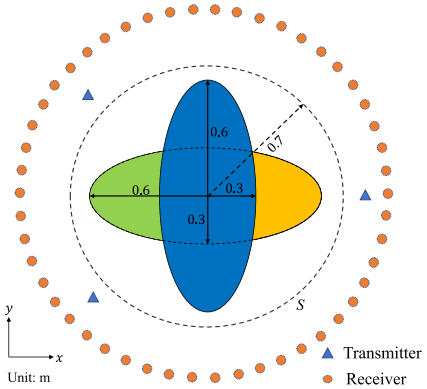

Fig. 2. Two overlapped dielectric anisotropic ellipses are illuminated by TE$_z$-polarized EM waves which are excited by three magnetic dipole transmitters. SIM is implemented on the smooth circular boundary S. The EM fields in the inhomogeneous region inside S are evaluated by SEM.

TABLE I
MODEL PARAMETERS OF TWO OVERLAPPED ANISOTROPIC ELLIPSES

Part \ Parameter	ε_x	ε_y	σ_x	σ_y	θ
left part of horizontal ellipse	2.6	1.8	10	4.0	$\pi/6$
right part of horizontal ellipse	1.4	3.0	5.0	12	$-\pi/4$
vertical ellipse	2.0	2.5	7.0	8.0	$\pi/3$

Remark: the unit of σ is mS/m; the unit of θ is rad.

D. Implementation of FWI

Once the sensitivity matrix is obtained, we first separate its real and imaginary parts to form the real sensitivity matrix. In this way, we can directly reconstruct the real relative permittivity, conductivity, and the rotation angle θ. Then, we follow the same procedure presented in Section II-D of [31] and construct the least square cost function. Finally, the CG method is adopted to minimize the cost function. In addition, the structural consistency constraint (SCC) is used to filter out the clutters of the background medium during the iteration process. Note the basic principle of SCC is to classify whether a discretized mesh inside the inversion domain is the "background" or "scatterer" based on maximum likelihood estimation. Its detailed algorithms and performance have been presented and verified in [14] and [31] and will not be repeated here.

III. FORWARD VALIDATION

In this section, we show the computation efficiency superiority of the proposed hybrid SESI solver to the traditional FEM which is implemented by the commercial software COMSOL via comparing their numerical simulation results. Both the EM scattering configuration and the basic geometry information are illustrated in Fig. 2. The SIM is implemented on the circular boundary S which is denoted by the black dotted line and has a radius of 0.7 m. Three magnetic dipole transmitters are located at $(-1.0, 0.0)$, $(-0.5, 0.866)$, and $(-0.5, -0.866)$ m. Totally, 50 receivers are evenly placed on a circle with a radius of 1.2 m. The scatterers include two overlapped anisotropic ellipses and their dielectric parameters are listed in Table I. The background is free space and the operation frequency is 1 GHz. To reliably simulate the tangential EM

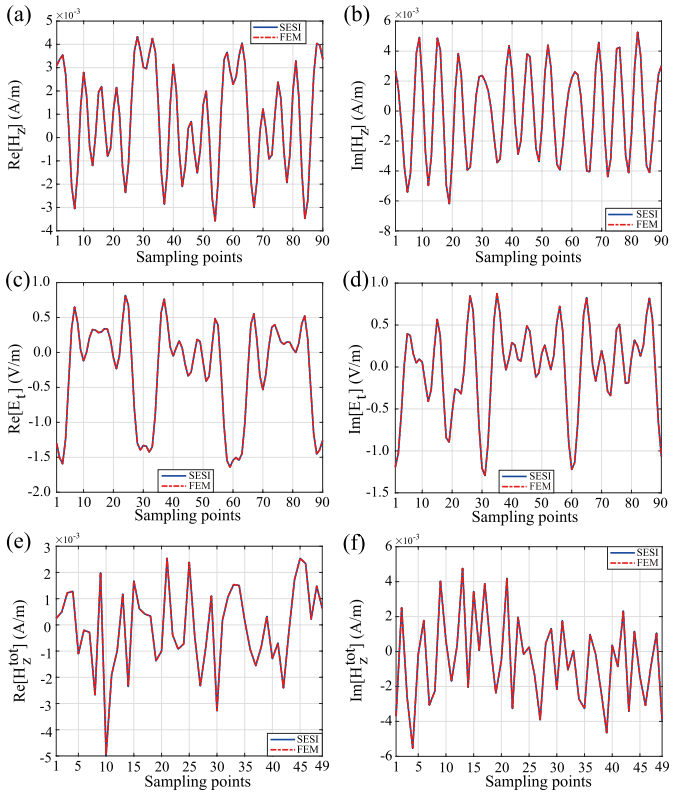

Fig. 3. Comparisons of the tangential EM fields along the circular boundary and the total magnetic fields inside the forward scattering computation domain computed by FEM and the hybrid SIM/SEM. (a) Real part of H_z. (b) Imaginary part of H_z. (c) Real part of E_t. (d) Imaginary part of E_t. (e) Real part of H_z^{tot}. (f) Imaginary part of H_z^{tot}.

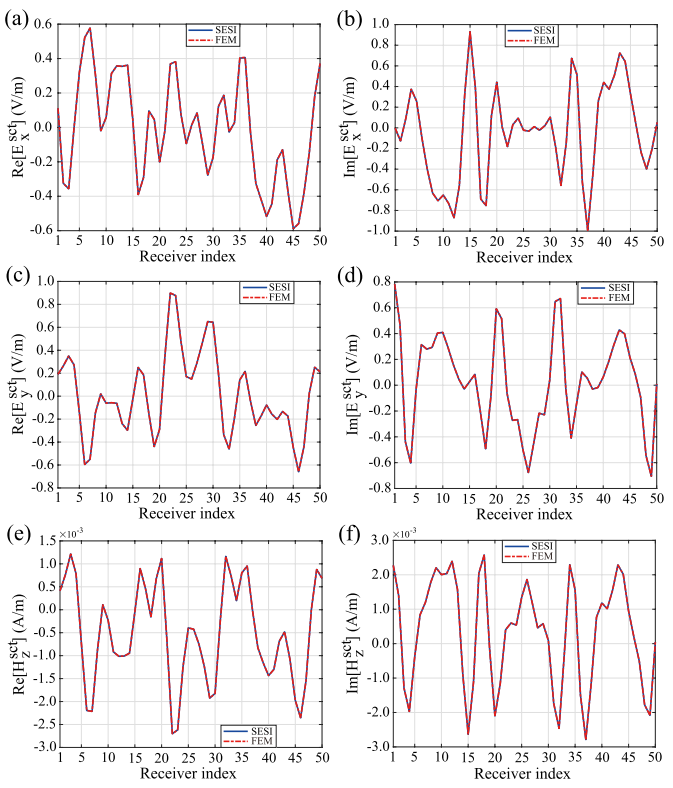

Fig. 4. Comparisons of the scattered EM fields at the receiver array computed by FEM and the hybrid SIM/SEM. (a) Real part of E_x^{sct}. (b) Imaginary part of E_x^{sct}. (c) Real part of E_y^{sct}. (d) Imaginary part of E_y^{sct}. (e) Real part of H_z^{sct}. (f) Imaginary part of H_z^{sct}.

fields on the boundary S, the total fields inside the computational domain, and the scattered fields at the receiver array by COMSOL, we set its square computational domain as large as 3.0 × 3.0 m with the perfectly matched layers (PMLs) to truncate it. Meanwhile, we set the SD for COMSOL simulation as 32.6 points per wavelength (PPW). By contrast, the SD for the second-order SEM implemented inside the computational domain is 16.7 PPW and it is 6.1 PPW on S for SIM. All the simulations and numerical computations are performed on a workstation with an 18-core I9-10980XE 3.0 G CPU and 256 GB RAM.

Fig. 3(a)–(d) shows comparisons of the tangential EM fields which are sampled at 90 points along the boundary S with the azimuthal angle equally divided. Note that E_t can be directly converted from the surface magnetic current. We can see the SESI results match the FEM results well. The relative error of H_z between SESI results and FEM results is 0.13% while the error of E_t is 0.16%. We then pick 7 × 7 uniform sampling points inside the computational domain and verify the accuracy of the total fields. The sampling point located at the bottom left corner has the coordinate of $(-0.45, -0.45)$ m. The increment between two sampling points in either the $\hat{x}$- or $\hat{y}$-direction is 0.15 m. Fig. 3(e)–(f) shows comparisons of the total magnetic fields at these sampling points computed by the hybrid SESI method and FEM. The relative error of H_z^{tot} between the two methods is 0.26%. Obviously, the SESI method can also reach a reliable accuracy for the computation of total fields.

Fig. 4 shows comparisons of the scattered EM fields at the receiver array computed by the hybrid SESI method and by FEM. The relative errors of E_x^{sct}, E_y^{sct}, and H_z^{sct} between SESI results and FEM results are 0.18%, 0.16%, and 0.18%, respectively. Although they have good matches, COMSOL takes 49 s and has a memory cost of 16.5 GB, while the hybrid SESI method only takes 9.2 s and 4.4 GB of memory to accomplish the calculation. This big discrepancy indicates that the proposed forward solver based on the hybrid SIM/SEM can achieve the same computation accuracy as that of the mature commercial software with a much lower cost.

IV. Inversion Assessment

In this section, we verify the feasibility of EM FWI based on the proposed hybrid SESI solver when the excitation source is TE_z-polarized. Note we use plane waves instead of the magnetic dipole to illuminate the inversion domain. In both numerical examples, the anisotropic dielectric parameters are reconstructed not only when the scattered electric fields are noise-free, but also when they are contaminated by 20 dB white Gaussian noise which leads to approximately 10% errors. Here, the noise level is defined according to the signal-to-noise ratio (SNR) of power. In the first numerical example, only the biaxially anisotropic dielectric parameters of two inhomogeneous scatterers are reconstructed. By contrast, in the second numerical example, not only the biaxial parameters are inverted, but also the rotation angles of the optical axes are simultaneously retrieved for two arbitrary anisotropic

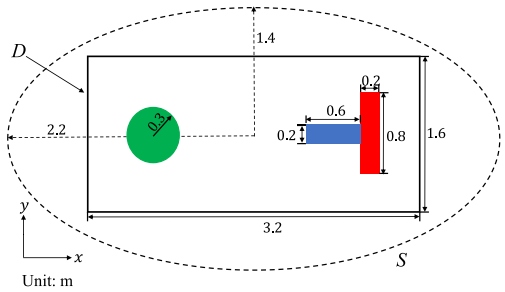

Fig. 5. Configuration of the 2-D inverse scattering model including a biaxially anisotropic homogeneous circular disk and a biaxially anisotropic inhomogeneous "T"-shaped scatterer. Their geometry sizes are annotated in the figure. The FWI is implemented in the rectangular region D.

TABLE II
MODEL PARAMETERS OF TWO BIAXIALLY ANISOTROPIC SCATTERERS

Part \ Parameter	ε_x	ε_y	σ_x	σ_y
circular disk	2.0	1.4	6.0	3.0
horizontal bar	2.4	1.8	10	6.0
vertical bar	1.6	2.2	2.0	9.0

Remark: the unit of σ is mS/m.

scatterers. In addition, to quantitatively evaluate the inversion performance, we define the data misfit to indicate the relative difference between the computed and measured scattered fields at the receiver array and the model misfit to indicate the relative difference between the reconstructed dielectric parameters and the true parameters in all the discretized elements inside the inversion domain. They are, respectively, expressed as

$$Err_{\text{data}} = \frac{\left\|\mathbf{f}_{inv}^{sct} - \mathbf{f}_{mea}^{sct}\right\|}{\left\|\mathbf{f}_{mea}^{sct}\right\|} \tag{34a}$$

$$\begin{aligned} Err_{\text{model}} &= 1 - \text{SSIM}(\mathbf{m}_{inv}, \mathbf{m}_{true}) \\ &= 1 - \frac{[2\overline{m}_{inv}\overline{m}_{true} + C_1][2\text{conv}(\mathbf{m}_{inv}, \mathbf{m}_{true}) + C_2]}{\left[\overline{m}_{inv}^2 + \overline{m}_{true}^2 + C_1\right]\left[S_{inv}^2 + S_{true}^2 + C_2\right]} \end{aligned} \tag{34b}$$

where $\|\cdot\|$ stands for the L_2 norm, $\mathbf{f}_{inv}^{sct}$ is a column vector containing the computed scattered field data sampled at the receiver array in the inversion iteration while $\mathbf{f}_{mea}^{sct}$ contains the measured scattered field data sampled at the receiver array, $\mathbf{m}_{inv}$ is a column vector containing the reconstructed model parameters of all the discretized elements inside the inversion domain while $\mathbf{m}_{true}$ contains the true model parameters of all discretized elements inside the inversion domain, $\overline{m}_{inv}$ is the mean of $\mathbf{m}_{inv}$ while $\overline{m}_{true}$ is the mean of $\mathbf{m}_{true}$, S_{inv} is the sample standard deviation of $\mathbf{m}_{inv}$ while S_{true} is the sample standard deviation of $\mathbf{m}_{true}$, and $\text{conv}(\mathbf{m}_{inv}, \mathbf{m}_{true})$ is the sample covariance of $\mathbf{m}_{inv}$ and $\mathbf{m}_{true}$. C_1 and C_2 are regularization constants to guarantee computation stability of the structural similarity index measure (SSIM) whose choices have been discussed in [38]. They are set as the square of one percent of the maximum absolution value of the true model parameters in the whole inversion domain.

A. Two Biaxially Anisotropic Scatterers

As shown in Fig. 5, a homogeneous circular disk and an inhomogeneous "T"-shaped scatterer are placed inside a rectangular inversion domain D with the size of 3.2 × 1.6 m which is uniformly discretized into 160 × 80 elements. The size of each square element is 0.02 × 0.02 m. The geometry sizes of two scatterers are annotated in Fig. 5 and their respective dielectric parameters are listed in Table II. The rectangular inversion domain is wrapped by an ellipse on which the SIM is performed. The horizontal half axis of the ellipse has a length of 2.2 m while the length of its vertical half axis is 1.4 m. We use 50 plane waves to illuminate the inversion domain and the incident directions of these waves evenly divide the whole circumference with equal azimuthal angle step. Meanwhile, 70 receivers evenly placed on a circle with a radius of 3.0 m are used to record the scattered electric fields. The operating frequency is 300 MHz.

TABLE III
MODEL MISFITS (%) OF FOUR RECONSTRUCTED BIAXIALLY ANISOTROPIC PARAMETERS WHEN ITERATIONS TERMINATE

SNR \ Parameter	ε_x	ε_y	σ_x	σ_y
Noise free	3.2	3.8	4.7	4.4
20 dB Noise	6.0	7.8	12.2	14.5

Fig. 6 shows ground truths of the dielectric parameters of two biaxially anisotropic scatterers and the corresponding inversion results when noise-free and the scattered electric fields are contaminated by 20-dB noise. The CG iteration terminates after 120 steps when the data misfit reaches 3.4×10^{-4} for the noise-free situation. However, it only takes 65 steps to accomplish the inversion when the data misfit reaches 9.9×10^{-2} for the noisy situation. The corresponding model misfit values when the iterations terminate are listed in Table III. By comparing the second column and the third column shown in Fig. 6, we can see the reconstructed shapes are clearly discernible and the obtained dielectric parameters are basically correct even when the scattered electric fields are contaminated by 20-dB noise. This indicates that the FWI based on the proposed hybrid SESI solver has a certain antinoise ability. Another observation is that the reconstructed shapes of permittivity distribution are closer to the true shape than those of conductivity distribution for the case with 20-dB noise. This is also manifested by the larger model misfit values of the reconstructed conductivity compared to those of the reconstructed permittivity listed in Table III. One possible reason for this phenomenon is that the imaginary part of the complex permittivity is obviously smaller than the real part, thus the scattered electric field is less sensitive to scatterer conductivity.

B. Two Arbitrary Anisotropic Scatterers

In this numerical example, we will reconstruct 2-D arbitrary anisotropic scatterers using SESI-CG. We rotate the optical axis to construct the arbitrary anisotropic dielectric parameters from biaxially anisotropic ones. Not only the biaxial parameters are reconstructed, but also the rotation angle is retrieved. As shown in Fig. 7, two homogeneous square scatterers have the same biaxial dielectric parameters $\varepsilon_x = 2.0$, $\varepsilon_y = 1.5$, $\sigma_x = 5.0$ mS/m, and $\sigma_y = 10$ mS/m before we rotate their

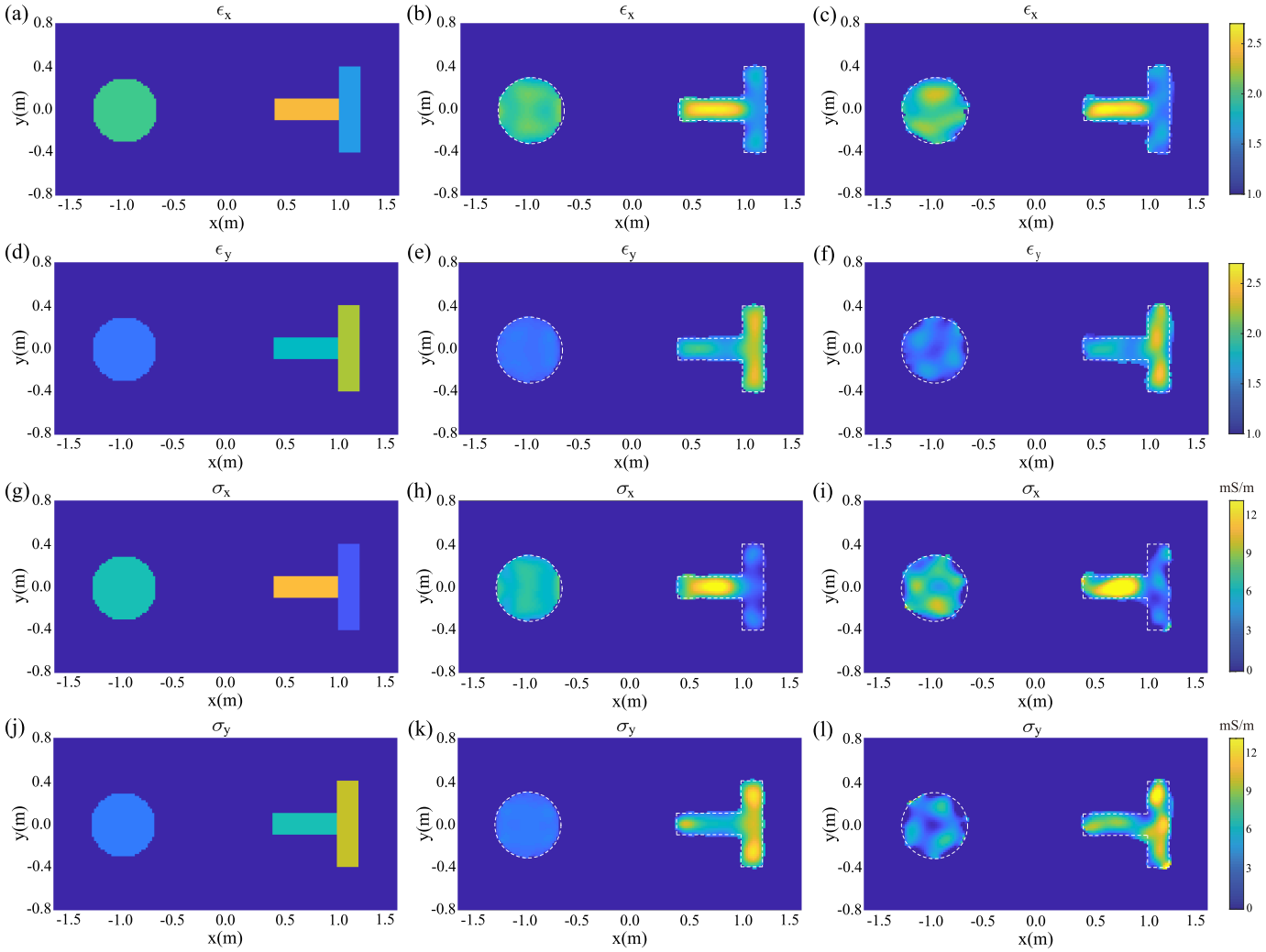

Fig. 6. Reconstructed biaxially anisotropic profiles of the 2-D scatterers. The first column shows the ground-truth profiles. The second column shows the reconstructed profiles when noise-free. The third column shows the reconstructed profiles when 20-dB noise is added. White dotted boxes denote true shapes.

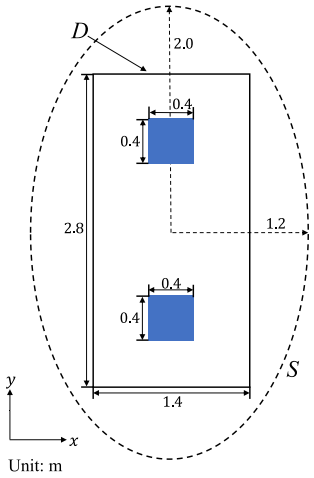

Fig. 7. Configuration of the 2-D inverse scattering model including two arbitrary anisotropic homogeneous square scatterers. Their geometry sizes are annotated in the figure. The FWI is implemented in the rectangular region D.

optical axes. We then let the rotation angle defined in (3) be $\pi/6$ for the upper square scatterer and that be $-\pi/6$ for the lower square scatterer to form two different arbitrary anisotropic scatterers. Other geometry sizes of the scatterers, inversion domain D, and the ellipse are also annotated in Fig. 7 and will not be repeated here. The rectangle inversion domain D is uniformly discretized into 70×140 elements and each square element has the size of 0.02×0.02 m. In total, 50 plane waves whose incident directions evenly divide the whole circumference with the equal azimuthal angle step are used to illuminate the inversion domain. And totally 60 receivers are evenly placed on a circle with a radius of 2.5 m. The operating frequency is still 300 MHz.

Fig. 8 shows the ground truth of the arbitrary anisotropic parameter distribution and the inversion results when the scattered electric fields recorded at the receiver array are noise-free or contaminated by 20-dB noise. Three observations are made here. First, SESI-CG can simultaneously reconstruct five arbitrary anisotropic parameters. Even when 20-dB noise is added, reliable inversion results still can be acquired. Second, the reconstructed rotation angles have worse profiles than those of biaxial permittivity and conductivity. This is further confirmed by the large model misfits of the reconstructed rotation angles when the iterations terminate as listed in Table IV. This may be because the derivatives of the arbitrary anisotropic parameters

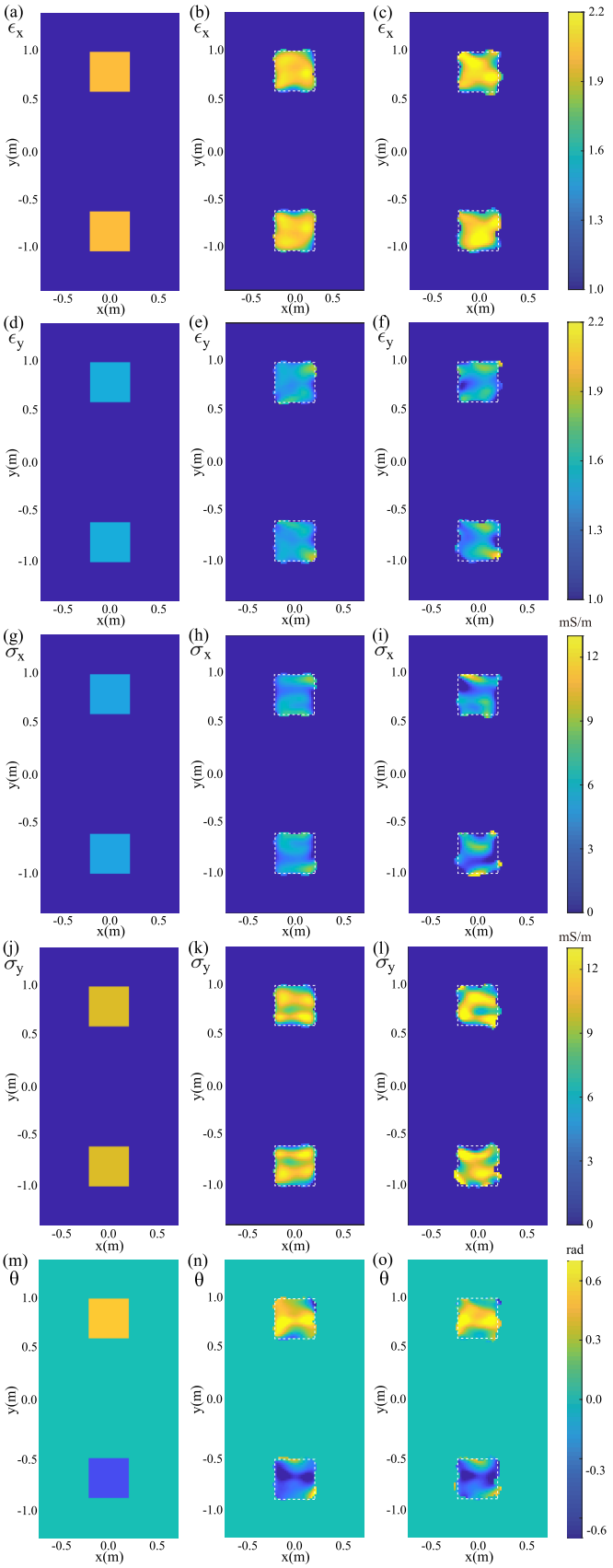

Fig. 8. Reconstructed dielectric biaxial parameters and optical axis rotation angles of the 2-D arbitrary anisotropic scatterers. The first column shows the ground-truth profiles. The second column shows the reconstructed profiles when noise-free. The third column shows the reconstructed profiles with 20-dB noise.

TABLE IV

MODEL MISFITS (%) OF FIVE RECONSTRUCTED ARBITRARY ANISOTROPIC PARAMETERS WHEN SESI-CG ITERATIONS TERMINATE

SNR \ Parameter	ε_x	ε_y	σ_x	σ_y	θ
Noise free	4.0	7.6	12.4	5.1	24.2
20 dB Noise	10.0	11.6	23.8	11.8	46.4

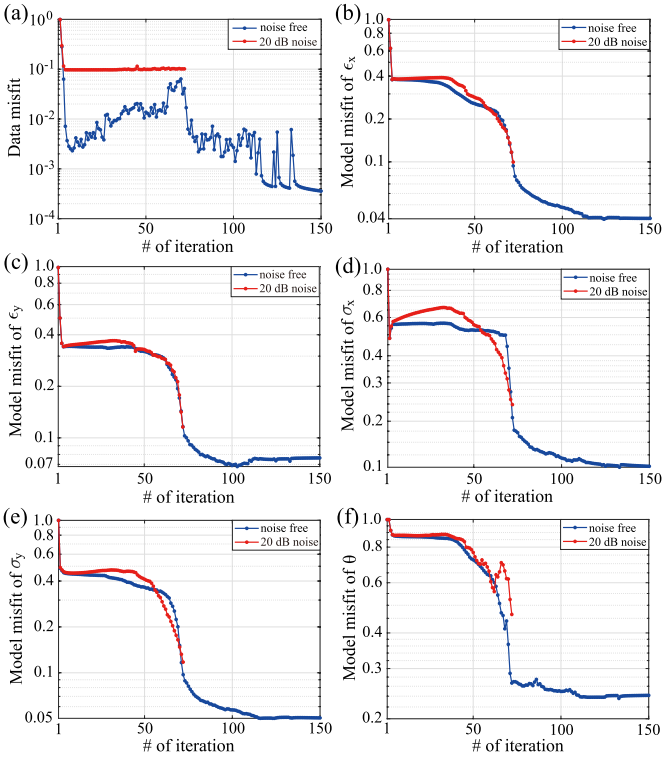

Fig. 9. The convergence processes for the FWI of the arbitrary anisotropic scatterers. (a) Variations of data misfits of the scattered fields in different iteration steps. (b) Variations of model misfits of ε_x in different iteration steps. (c) Variations of model misfits of ε_y in different iteration steps. (d) Variations of model misfits of σ in different iteration steps. (e) Variations of model misfits of σ_y in different iteration steps. (f) Variations of model misfits of θ in different iteration steps.

with respect to the rotation angle are more complicated than those with respect to a single biaxial parameter, as illustrated in (29c). The complicated expressions of derivatives naturally increase the nonlinearity, nonuniqueness, and instability of the inversion. Third, compared with the inversion results shown in Fig. 6 for biaxial anisotropic scatterers, the reconstructed profiles shown in the first four rows of Fig. 8 are obviously worse. The rotation of the optical axes actually strengthens the nonlinearity relationship between the dielectric parameters and the scattered fields, which automatically deteriorates the inversion performance.

Fig. 9(a) shows the variations of data misfits in different SESI-CG iteration steps. We can see that the CG solver takes 150 steps until the data misfit becomes less than 0.04% to stop when noise-free. However, it only takes 72 steps to terminate if the relative error in three constitutive steps is less than

0.1% for the noisy case. The data misfit value then weakly fluctuates up and down in the noise level and almost remains unchanged. Fig. 9(b)–(f) shows the variations of model misfits of five anisotropic parameters in corresponding iteration steps. We can see the convergence curves for the noise-free case and for the case with 20-dB noise almost overlap in a series of iteration steps. However, the final model misfits for the noise-free case are definitely lower than those for the noisy case.

V. Conclusion and Summary

In this work, we developed the hybrid SESI method for EM scattering from 2-D anisotropic scatterers when the excitation source is TE_z-polarized. The inhomogeneous region is discretized and solved by SEM whose computational domain is truncated by a smooth elliptical boundary on which SIM is implemented to realize the RBC. Then the discretized state equation is formed and both the spatial-domain magnetic field in the internal nodes and the Fourier coefficients of equivalent electric current and magnetic current on the smooth boundary can be simultaneously solved. Finally, the spatial-domain scattered EM fields at the receiver array can be directly computed by multiplying the Fourier coefficients on the boundary and the spectral-domain radiation matrix. For the inversion, to assemble the sensitivity matrix, we first compute the adjoint magnetic fields by multiplying the conjugate transpose of the old system matrix by the system matrix itself to form a new system matrix. Then, we focus on the stiffness part of the old system matrix and compute its first-order derivative with respect to the anisotropic model parameters inside the inversion domain. Finally, we multiply the adjoint magnetic field solution by the derivative matrix of the stiffness matrix and multiply them by the magnetic field solution itself to obtain the final sensitivity matrix.

Several numerical examples are given to show the computation efficiency of the proposed hybrid SEIM/SEM for forward scattering and its feasibility for inverse scattering. It is found that not only the computation time, but also the memory cost is significantly reduced by the hybrid SISE method compared to the traditional FEM in the forward scattering. In the inversion, numerical results show that SESI-CG can reconstruct all anisotropic model parameters including the optical axis rotation angle. However, the obtained parameter profiles show some fluctuations within homogeneous regions and this phenomenon becomes more severe when the measured scattered field data are contaminated by 20-dB noise.

References

[1] L. Tsang, K.-H. Ding, S. Huang, and X. Xu, "Electromagnetic computation in scattering of electromagnetic waves by random rough surface and dense media in microwave remote sensing of land surfaces," *Proc. IEEE*, vol. 101, no. 2, pp. 255–279, Feb. 2013.

[2] C. Liu and L. C. Shen, "Numerical simulation of subsurface radar for detecting buried pipes," *IEEE Trans. Geosci. Remote Sens.*, vol. 29, no. 5, pp. 795–798, Sep. 1991.

[3] M. Dehmollaian, N. Chamanara, and C. Caloz, "Wave scattering by a cylindrical metasurface cavity of arbitrary cross section: Theory and applications," *IEEE Trans. Antennas Propag.*, vol. 67, no. 6, pp. 4059–4072, Jun. 2019.

[4] Y. Chu et al., "Fast microwave through wall imaging method with inhomogeneous background based on Levenberg–Marquardt algorithm," *IEEE Trans. Microw. Theory Techn.*, vol. 67, no. 3, pp. 1138–1147, Mar. 2019.

[5] C. Qiu, B. Liang, F. Han, J. Li, G. Fang, and Q. H. Liu, "3-D full-wave inversion of helicopter transient electromagnetic data in frequency domain," *IEEE Trans. Geosci. Remote Sens.*, vol. 58, no. 7, pp. 4928–4938, Jul. 2020.

[6] R. Hong et al., "3-D MRI-based electrical properties tomography using the volume integral equation method," *IEEE Trans. Microw. Theory Techn.*, vol. 65, no. 12, pp. 4802–4811, Dec. 2017.

[7] J. Richmond, "Scattering by a dielectric cylinder of arbitrary cross section shape," *IEEE Trans. Antennas Propag.*, vol. AP-13, no. 3, pp. 334–341, May 1965.

[8] A. Glisson and D. Wilton, "Simple and efficient numerical methods for problems of electromagnetic radiation and scattering from surfaces," *IEEE Trans. Antennas Propag.*, vol. AP-28, no. 5, pp. 593–603, Sep. 1980.

[9] G. K. Avdikos and H. T. Anastassiu, "Computational cost estimations and comparisons for three methods of applied electromagnetics (MoM, MAS, MMAS)," *IEEE Antennas Propag. Mag.*, vol. 47, no. 1, pp. 121–129, Feb. 2005.

[10] Y. Hua Zhang, B. Xun Xiao, and G. Qiang Zhu, "An improved weak-form BCGS-FFT combined with DCIM for analyzing electromagnetic scattering by 3-D objects in planarly layered media," *IEEE Trans. Geosci. Remote Sens.*, vol. 44, no. 12, pp. 3540–3546, Dec. 2006.

[11] N. Engheta, W. D. Murphy, V. Rokhlin, and M. S. Vassiliou, "The fast multipole method (FMM) for electromagnetic scattering problems," *IEEE Trans. Antennas Propag.*, vol. 40, no. 6, pp. 634–641, Jun. 1992.

[12] E. Bleszynski, M. Bleszynski, and T. Jaroszewicz, "AIM: Adaptive integral method for solving large-scale electromagnetic scattering and radiation problems," *Radio Sci.*, vol. 31, no. 5, pp. 1225–1251, Sep. 1996.

[13] X.-C. Nie, L.-W. Li, N. Yuan, T. Soon Yeo, and Y.-B. Gan, "Precorrected-FFT solution of the volume integral equation for 3-D inhomogeneous dielectric objects," *IEEE Trans. Antennas Propag.*, vol. 53, no. 1, pp. 313–320, Jan. 2005.

[14] J. Zhuo, L. Ye, F. Han, L. Xiong, and Q. H. Liu, "Multiparametric electromagnetic inversion of 3-D biaxial anisotropic objects embedded in layered uniaxial media using VBIM enhanced by structural consistency constraint," *IEEE Trans. Antennas Propag.*, vol. 68, no. 6, pp. 4774–4785, Jun. 2020.

[15] J. Li, J. Zhuo, Z. Guan, F. Han, and Q. H. Liu, "3-D electromagnetic scattering and inverse scattering by magnetodielectric objects with arbitrary anisotropy in layered uniaxial media," *IEEE Trans. Antennas Propag.*, vol. 68, no. 2, pp. 1009–1022, Feb. 2020.

[16] J. Wang, J. Li, Y. Chen, F. Han, and Q. H. Liu, "Simulation of 3-D electromagnetic scattering and inverse scattering by arbitrary anisotropic dielectric objects embedded in layered arbitrary anisotropic media," *IEEE Trans. Antennas Propag.*, vol. 68, no. 8, pp. 6473–6478, Aug. 2020.

[17] B. Liang et al., "A new inversion method based on distorted Born iterative method for grounded electrical source airborne transient electromagnetics," *IEEE Trans. Geosci. Remote Sens.*, vol. 56, no. 2, pp. 877–887, Feb. 2018.

[18] P. M. V. D. Berg and R. E. Kleinman, "A contrast source inversion method," *Inverse Problems*, vol. 13, no. 6, pp. 1607–1620, Dec. 1997.

[19] P. M. V. D. Berg, A. L. V. Broekhoven, and A. Abubakar, "Extended contrast source inversion," *Inverse Problems*, vol. 15, no. 5, pp. 1325–1344, Oct. 1999.

[20] X. Chen, "Subspace-based optimization method for solving inverse-scattering problems," *IEEE Trans. Geosci. Remote Sens.*, vol. 48, no. 1, pp. 42–49, Jan. 2010.

[21] J. Xie et al., "3-D magnetotelluric inversion and application using the edge-based finite element with hexahedral mesh," *IEEE Trans. Geosci. Remote Sens.*, vol. 60, 2022, Art. no. 4503011.

[22] Z. Wu, Y. Fan, J. Wang, R. Zhang, and Q. H. Liu, "Application of 2.5-D finite difference method in logging-while-drilling electromagnetic measurements for complex scenarios," *IEEE Geosci. Remote Sens. Lett.*, vol. 17, no. 4, pp. 577–581, Apr. 2020.

[23] M. Weiss, T. Kalscheuer, and Z. Ren, "Spectral element method for 3-D controlled-source electromagnetic forward modelling using unstructured hexahedral meshes," *Geophys. J. Int.*, vol. 232, no. 2, pp. 1427–1454, Nov. 2022.

[24] D. Avdeev and A. Avdeeva, "3D magnetotelluric inversion using a limited-memory quasi-Newton optimization," *Geophysics*, vol. 74, no. 3, pp. F45–F57, May 2009.
[25] G. A. Newman, M. Commer, and J. J. Carazzone, "Imaging CSEM data in the presence of electrical anisotropy," *Geophysics*, vol. 75, no. 2, pp. F51–F61, Mar. 2010.
[26] W. Rodi and R. L. Mackie, "Nonlinear conjugate gradients algorithm for 2-D magnetotelluric inversion," *Geophysics*, vol. 66, no. 1, pp. 174–187, 2001.
[27] W. Siripunvaraporn and G. Egbert, "Data space conjugate gradient inversion for 2-D magnetotelluric data," *Geophys. J. Int.*, vol. 170, no. 3, pp. 986–994, Sep. 2007.
[28] A. Abubakar, T. M. Habashy, V. L. Druskin, L. Knizhnerman, and D. Alumbaugh, "2.5D forward and inverse modeling for interpreting low-frequency electromagnetic measurements," *Geophysics*, vol. 73, no. 4, pp. F165–F177, Jul. 2008.
[29] H. Jahandari and C. G. Farquharson, "3-D minimum-structure inversion of magnetotelluric data using the finite-element method and tetrahedral grids," *Geophys. J. Int.*, vol. 211, no. 2, pp. 1189–1205, Nov. 2017.
[30] Z. Guan, J. Liu, M. Zhuang, and Q. H. Liu, "A hybrid SESI method for electromagnetic scattering by objects in multiregion cylindrically layered media," *IEEE Trans. Microw. Theory Techn.*, vol. 69, no. 9, pp. 3967–3975, Sep. 2021.
[31] J. Li, Z. Guan, J. Wang, L.-Y. Xiao, and Q. H. Liu, "Contracting electromagnetic full-wave inversion of 2-D inhomogeneous objects with irregular shapes based on the hybrid SESI forward solver," *IEEE Trans. Geosci. Remote Sens.*, vol. 60, 2022, Art. no. 5305411.
[32] K. Agarwal, L. Pan, and X. Chen, "Subspace-based optimization method for reconstruction of 2-D complex anisotropic dielectric objects," *IEEE Trans. Microw. Theory Techn.*, vol. 58, no. 4, pp. 1065–1074, Apr. 2010.
[33] X. Ye et al., "Application of subspace-based distorted-Born iteration method in imaging biaxial anisotropic scatterer," *IEEE Trans. Comput. Imag.*, vol. 6, pp. 1486–1492, 2020.
[34] Y. Liu et al., "A frequency-hopping subspace-based optimization method for reconstruction of 2-D large uniaxial anisotropic scatterers with TE illumination," *IEEE Trans. Geosci. Remote Sens.*, vol. 54, no. 10, pp. 6091–6099, Oct. 2016.
[35] Z. Guan, J. Li, and F. Han, "Exponential accuracy solutions of 2-D electromagnetic scattering from multilayered nonconcentric elliptical magnetodielectric cylinders under TE illumination," *IEEE Trans. Microw. Theory Techn.*, early access, Sep. 26, 2023, doi: 10.1109/TMTT.2023.3320733.
[36] J.-H. Lee, T. Xiao, and Q. H. Liu, "A 3-D spectral-element method using mixed-order curl conforming vector basis functions for electromagnetic fields," *IEEE Trans. Microw. Theory Techn.*, vol. 54, no. 1, pp. 437–444, Jan. 2006.
[37] F. Q. Hu, "A spectral boundary integral equation method for the 2D Helmholtz equation," *J. Comput. Phys.*, vol. 120, no. 2, pp. 340–347, Sep. 1995.
[38] Z. Wang, A. C. Bovik, H. R. Sheikh, and E. P. Simoncelli, "Image quality assessment: From error visibility to structural similarity," *IEEE Trans. Image Process.*, vol. 13, no. 4, pp. 600–612, Apr. 2004.

Jiawen Li received the B.S. degree in electronic science and technology from the Wuhan University of Technology of China, Wuhan, China, in 2011, and the Ph.D. degree in electromagnetic field and microwave technology from the Xiamen University, Xiamen, China, in 2023.

Since August 2023, he has been with Guangxi Normal University, Guangxi, China, where he is currently an Assistant Professor with the School of Electronic and Information Engineering. His research interests include electromagnetic scattering and inverse scattering in complex media and the full-wave inversion of anisotropic targets.

Zili Li received the Ph.D. degree in communication and information systems from the School of Electronic Information, Wuhan University, Wuhan, China, in 2010.

Since July 2010, he has been with Guangxi Normal University, Guangxi, China, where he is currently an Associate Professor with the School of Electronic and Information Engineering. His research interests include the fast algorithms for computational electromagnetics, electromagnetic scattering, and electromagnetic remote sensing technologies and their applications.

Zhen Guan received the Ph.D. degree in computational science from the School of Mathematical Sciences and the Institute of Electromagnetics and Acoustics, Xiamen University, Xiamen, China, in 2022.

From March 2021 to April 2022, she was a Joint-Training Ph.D. Student with the Mathematical Institute, Department of Mathematics and Computer Science, Free University Berlin, Berlin, Germany. Since July 2022, she has been with the Tianjin University of Technology, Tianjin, China, where she is currently a Lecturer with the School of Science. Her research interests include the fast algorithms for computational electromagnetics and electromagnetic scattering and inverse scattering problems and their applications in engineering.

Feng Han (Senior Member, IEEE) received the B.S. degree in electronic science from Beijing Normal University, Beijing, China, in 2003, the M.S. degree in geophysics from Peking University, Beijing, in 2006, and the Ph.D. degree in electrical engineering from Duke University, Durham, NC, USA, in 2011.

From 2011 to 2015, he was a Software Engineer at Wavenovation Inc., Xiamen, China. In July 2015, he joined the Institute of Electromagnetics and Acoustics, Xiamen University, Xiamen as an Assistant Professor, and was promoted to Associate Professor there in 2020. In October 2023, he joined the School of Computing and Information Technology, Great Bay University, Guangdong, China, as an Associate Professor. He has published over 50 articles in refereed journals. His research interests include electromagnetic scattering and inverse scattering in complex media, multiparametric and multidimensional hybrid electromagnetic full-wave inversion, fast electromagnetic full-wave inversion based on scientific machine learning, configuration of the antenna array for electromagnetic inverse problems, and geophysical electromagnetic exploration and inversion.